Observation of Weyl Interface States in Non-Hermitian Synthetic Photonic Systems

Wange Song[1], Shengjie Wu,[1] Chen Chen,[1] Yuxin Chen,[1] Chunyu Huang,[1]
Luqi Yuan[2,*] Shining Zhu,[1] and Tao Li[1,†]

[1]*National Laboratory of Solid State Microstructures, Key Laboratory of Intelligent Optical Sensing and Integration, Jiangsu Key Laboratory of Artificial Functional Materials, College of Engineering and Applied Sciences, Nanjing University, Nanjing 210093, China*
[2]*State Key Laboratory of Advanced Optical Communication Systems and Networks, School of Physics and Astronomy, Shanghai Jiao Tong University, Shanghai 200240, China*

Weyl medium has triggered remarkable interest owing to its nontrivial topological edge states in 3D photonic band structures that were mainly revealed as surface modes yet. It is undoubted that the connection of two different Weyl media will give rise to more fruitful physics at their interface, while they face extreme difficulty in high-dimensional lattice matching. Here, we successfully demonstrate the non-Hermitian Weyl interface physics in *complex synthetic parameter space*, which is implemented in a loss-controlled silicon waveguide array. By establishing non-Hermitian Hamiltonian in the parameter space, new Weyl interfaces with distinct topological origins are predicted and experimentally observed in silicon waveguides. Significantly, our Letter exploits the non-Hermitian parameter to create the *synthetic dimension* by manipulating the *non-Hermitian order*, which successfully circumvents the difficulty in lattice matching for high-dimensional interfaces. The revealed rich topological Weyl interface states and their phase transitions in silicon waveguide platform further imply potentials in chip-scale photonics integrations.

Topological photonics has triggered considerable interest in realizing symmetry-protected edge states that imply potential applications in robust photonics integrations [1,2]. In recent years, in pursuit of richer physics people has paid more attention to higher-dimensional topological systems, where the 3D photonic analog of topological semimetal gives rise to the photonic Weyl point (WP). The WP is a degeneracy point of 3D band structure with linear dispersion in the momentum space, and has attracted increasing attention with the emergence of topological modes known as the Fermi arc surface states [3–13]. Specially, a broad range of interest has been reignited in connection with non-Hermiticity that demonstrates complex Weyl structures and unconventional topological effects [14–20]. For example, the non-Hermiticity would expand the Berry charge of the WP out onto a Weyl exceptional ring (WER) that shows completely distinct topological properties inside and outside the ring [14]. A pioneering experimental work has demonstrated the WER in helical waveguide arrays, and the non-Hermitian Fermi arc state is observed at the surface of a single Weyl medium [20]. However, connecting two media with distinct *topological order* will undoubtedly indicate more flexible topological channels (like *domain walls*) for light guiding, splitting, and robust light sources [21–25], etc. Following the trend from low to higher dimensions, it is quite promising to explore the domain walls formed by two independent non-Hermitian Weyl media, which, however, remains extremely challenging due to the difficulty in higher-dimensional lattice matching.

Fortunately, the newly emerging *synthetic dimension* shows a powerful way to manipulate the *topological order* by squeezing higher dimensions to lower ones [26–34], which provides new possibilities to explore Weyl physics [35–39]. One powerful approach for creating a higher-dimensional Hamiltonian is to utilize the parameter degrees of freedom, which can be mapped onto the synthetic momentum dimension in a Hamiltonian [29,36–39]. Recently, the parameter space is introduced in acoustics systems with gain or loss modulation to explore the WER [39], which focuses on a single Weyl structure. In that work [39], the parameter spaces are formed based on parameters in a Hermitian Hamiltonian, while the parameter associated to non-Hermitian contributions is treated as an additional term or perturbation on the original Hermitian system. In fact, the non-Hermitian parameter can be viewed as a new degree of freedom to control the interface modes [40–48]. It is of fundamental importance to extend the synthetic dimension by utilizing non-Hermitian parameters, which may empower people to flexibly manipulate the *non-Hermitian order* [49] in a topological system and provide new possibilities in inspecting non-Hermitian Weyl physics.

In this Letter, we investigate non-Hermitian Weyl interface states in a silicon waveguide array platform, where the

loss is controlled by the covered chromium (Cr). By synthesizing the waveguide widths, positions, and loss (deposited Cr) together, we propose a *complex synthetic parameter space*, where the Weyl degeneracies (WP and WER) are demonstrated. In particular, the non-Hermitian parameter (i.e., the arrangement of lossy components) has been taken to construct the synthetic dimension. In such complex synthetic parameter space, new interface Weyl states are discovered between two non-Hermitian structures, which can be distinguished by their locations at the synthetic space. We further design and fabricate the non-Hermitian silicon waveguide array in experiments, and observe the interface states in near-infrared wavelength. Our Letter exploits the non-Hermitian parameter to create the synthetic space and hence manipulate the *non-Hermitian order*, which demonstrates new Weyl interface states with solid confirmation in on-chip silicon waveguide experiments.

Figure 1(a) shows the schematics of the Si waveguide array with Cr stripes that follows a sinusoidal trajectory $x(z) = A \sin(2\pi/Pz + \varphi)$, where A, P, and φ are the bending amplitude, period, and initial phase. The cross section of a unit cell is shown at the bottom in Fig. 1(a), which consists of two waveguides with the widths defined as $w_1 = w_c(1 + l)$, $w_2 = w_c(1 - l)$, the gaps $d_1 = d_{1c}(1 + f_1 n)$, $d_2 = d_{2c}(1 - f_2 n)$, and the lattice constant $\Lambda = 2w_c + d_{1c} + d_{2c}$. Here, $w_c = 0.4$ μm, $f_i = (d_{1c} + d_{2c})/2d_{ic}$, where $d_{1c} = 0.480$ μm, and $d_{2c} = 0.193$ μm (gives alternating negative and positive couplings of the same strength with $A = 0.68$ μm and $P = 10$ μm, see Supplemental Material S1 [50]). The widths of the Cr are defined as $w_{Cr1} = w_{Crc}(1 + m)$, $w_{Cr2} = w_{Crc}(1 - m)$. Overall, l, m, and n are three independent numbers within $[-1, 1]$. l and n are two Hermitian parameters modulating the propagation constant and coupling coefficient, while m corresponds to the loss for the non-Hermiticity [54,55]. We can regard l and n as two Hermitian parameter spaces and m as the non-Hermitian parameter space, and when incorporating the 1D Bloch wave vector k along the transverse direction x, they
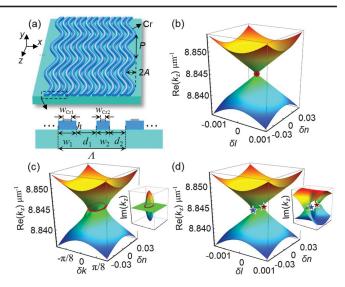

FIG. 1. (a) Schematics of the Cr-deposited curved silicon waveguides and the cross section of the unit cell. (b) Band structures in the $\delta l - \delta n$ synthetic space with $\delta k = 0$ for the Hermitian case. The WP is marked by the red dot. (c) Real part of the spectrum on $\delta k - \delta n$ space at $\delta l = 0$ in the non-Hermitian system. A WER is identified and marked by the red circle. The inset shows the corresponding imaginary part. (d) The same system viewed on $\delta l - \delta n$ space with $\delta k = 0$. The two EPs are marked by the pentagrams.

construct a complex synthetic-reciprocal space (l, m, n, k). For a straight waveguide array, a twofold degenerate point appears at $(l_c, m_c, n_c, k_c) = (0, 0, 0, \pi/\Lambda)$ [56]. By curving the waveguides, the alternating positive and negative coupling can shift the degenerate point to the center of the Brillouin zone $(l_c, m_c, n_c, k_c) = (0, 0, 0, 0)$, which makes it easier to realize the eigenmode [57–61] (see Supplemental Material S1 [50]).

We define four dimensionless coefficients $\delta l = l - l_c$, $\delta m = m - m_c$, $\delta n = n - n_c$, and $\delta k = (k - k_c)/k_0$ ($k_0 = \pi/\Lambda$) in the following derivation. By employing the tight-binding approximation, the Hamiltonian writes

$$H = [\beta_1(\delta l) + i\gamma_1(\delta m)]\sum_j a_{1,j}^\dagger a_{1,j} + [\beta_2(\delta l) + i\gamma_2(\delta m)]\sum_j a_{2,j}^\dagger a_{2,j}$$
$$+ \kappa_1(\delta n)\sum_j (a_{1,j}^\dagger a_{2,j} + a_{2,j}^\dagger a_{1,j}) + \kappa_2(\delta n)\sum_j (a_{1,j+1}^\dagger a_{2,j} + a_{2,j}^\dagger a_{1,j+1}), \tag{1}$$

where $\beta_{1(2)}(\delta l)$ and $\gamma_{1(2)}(\delta m)$ are the propagation constant and loss of the waveguides, respectively. $\kappa_{1(2)}(\delta n)$ represents coupling coefficient. Upon Fourier transformation and expanding H with respect to $(\delta l, \delta m, \delta n, \delta k)$ up to the first order, we finally get the effective Hamiltonian (see Supplemental Material S1 [50]):

$$H = c\delta n\sigma_x + K_0\delta k\sigma_y + (b\delta l + ia\delta m)\sigma_z + (\beta_0 + i\gamma_0)\sigma_0, \tag{2}$$

where σ_x, σ_y, and σ_z are Pauli matrices, σ_0 is a 2×2 identity matrix. $K_0 = k_0\Lambda\kappa_0$, $\beta_0 = 8.84445$ μm^{-1}, $\kappa_0 = 0.01$ μm^{-1}, $\gamma_0 = 0.02$ μm^{-1}, $b = 6.29321$ μm^{-1},

$c = 0.123 \ \mu m^{-1}$, and $a = 0.01991 \ \mu m^{-1}$. This Hamiltonian is a non-Hermitian variant of the standard Weyl Hamiltonian [14,20], which contains four real parameters: the momentum δk and parameters of δl, δm, and δn to mimic the synthetic momenta. Figure 1(b) shows the projection of the bulk bands in the $(\delta l, \delta n)$ space in the Hermitian limit ($\delta m = 0$). The degenerate point is a WP and its charge can be determined as sgn (cK_0b). If $\delta m \neq 0$, the non-Hermiticity is introduced that spawns the exceptional points (EPs) from the WP. Specifically, the WP morphs into a continuous closed trajectory on the $\delta K - \delta n$ plane, at which the real and imaginary parts of the eigenvalues are identical [Fig. 1(c)]. This circled trajectory is a Weyl exceptional ring (WER). Figure 1(d) shows the bands on the δl-δn cut plane at $\delta k = 0$, which intersect the WER at the two EPs marked by the pentagrams.

Different from previous works where the non-Hermitian parameter is considered as an additional perturbation [14,15,20,39], here we treat the non-Hermitian parameter δm as a new *synthetic dimension* and inspect the spectrum in the δl-δm space [see Fig. 2(b)]. Along the δm axis, the real part of the spectrum $\mathrm{Re}(k_z)$ is gapped for $-|\sqrt{(c\delta n)^2 + (K_0 \delta k)^2}/a| < \delta m < |\sqrt{(c\delta n)^2 + (K_0 \delta k)^2}/a|$
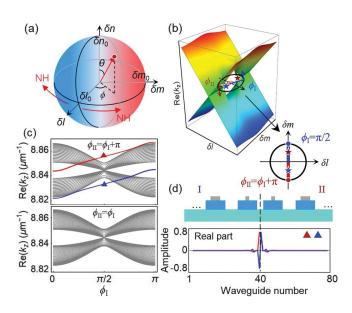

FIG. 2. (a) Rotational sphere in $\delta l - \delta m - \delta n$ parameter spaces. (b) Real part of the band structures in $\delta l - \delta m$ space. The EPs with opposite chirality are marked by the red and blue pentagrams. A projective rotational loop is introduced, where ϕ_I and ϕ_II are rotational angles that define the two synthetic Weyl media (I and II). Bottom: the positions of the two Weyl media at $\delta l - \delta m$ space for $\phi_\mathrm{I} = \pi/2$ and $\phi_\mathrm{II} = \phi_\mathrm{I} + \pi$. (c) Real part of the eigenvalue spectra as a function of ϕ_I for loops in (b), with $\phi_\mathrm{II} = \phi_\mathrm{I} + \pi$ (top) and $\phi_\mathrm{II} = \phi_\mathrm{I}$ (bottom). The red and blue curves are the interface modes and gray bands represent the bulk. (d) Schematics of the waveguide structure and field distributions (real part of the complex amplitude) of the interface states [marked by red and blue triangles in (c)]. The black dashed line indicates the interface and four central waveguides are enlarged.

and ungapped for $|\delta m| > |\sqrt{(c\delta n)^2 + (K_0 \delta k)^2}/a|$. There are two EPs at $[0, \pm|\sqrt{(c\delta n)^2 + (K_0 \delta k)^2}/a|]$ with opposite chirality separating the gapped and ungapped δm domains [62] [marked by pentagrams in Fig. 2(b)]. Tuning in the non-Hermitian parameter space δm gives rise to new Weyl states, as will be shown later.

After successfully mapping the high-dimensional non-Hermitian Weyl Hamiltonian into the 1D lossy waveguide array, we would like to construct a controllable interface between two Weyl structures. A rotational sphere around the Weyl degeneracy in the $\delta l - \delta m - \delta n$ parameter spaces is introduced [see Fig. 2(a)]:

$$\delta l = \delta l_0' \sin\theta \cos\phi \equiv \delta l_0 \cos\phi,$$
$$\delta m = \delta m_0' \sin\theta \sin\phi \equiv \delta m_0 \sin\phi,$$
$$\delta n = \delta n_0' \cos\theta \equiv \delta n_0, \qquad (3)$$

where θ and $\phi \in [0, 2\pi]$ are the polar and azimuthal angles of the parameter sphere, respectively, and $\delta l_0'$, $\delta m_0'$, $\delta n_0'$ are the radii. Each point on the sphere represents a Weyl medium with specific parameters. Consider an interface between two Weyl media (i.e., δl_I, δn_I, δm_I for medium I, and δl_II, δn_II, δm_II for medium II). According to Eq. (3), if δl_0, δm_0, and δn_0 are fixed, the two Weyl media can be solely defined by ϕ_I and ϕ_II for medium I and II, respectively. In fact, ϕ describes the projected loop on the $\delta l - \delta m$ plane, as shown in Fig. 2(b). Numerical calculations are carried out for the interfaced synthetic Weyl structure, in which $\delta l_0 = 0.001$, $\delta m_0 = 1$, $\delta n_0 = 0.01$, and the number of unit cells is set as 40 on each side. The eigenvalue spectrum as a function of ϕ_I demonstrates interface modes for $\phi_\mathrm{II} = \phi_\mathrm{I} + \pi$ [Fig. 2(c), top, red and blue curves], while none for $\phi_\mathrm{II} = \phi_\mathrm{I}$ [Fig. 2(c), bottom]. The emergence of the interface modes can be intuitively explained in that varying ϕ_II and ϕ_I modulates the "*mass*" term [1,62] in the Hamiltonian H [i.e., $b\delta l + ia\delta m$ in Eq. (2)], which is complex and denotes the real mass ($b\delta l$) and the imaginary mass ($a\delta m$). Notably, the case $\phi_\mathrm{II} = \phi_\mathrm{I}$ gives rise to the same mass ($\delta l_\mathrm{I} = \delta l_\mathrm{II}$ and $\delta m_\mathrm{I} = \delta m_\mathrm{II}$) for the two media, while $\phi_\mathrm{II} = \phi_\mathrm{I} + \pi$ leads to sign-reversal for the mass, which ensures the emergence of the interface modes [1,63,64]. Specifically, for $\phi_\mathrm{I} = 0$ case (i.e., $\delta l_\mathrm{I} = -\delta l_\mathrm{II}$, $\delta m_\mathrm{I} = \delta m_\mathrm{II} = 0$), which is analogous to having sign-reversed real mass (i.e., the conventional *topological order*), there is an interface mode inside the band gap corresponding to the Fermi arc like topological states generated by the WP. For the case of $\phi_\mathrm{I} = \pi/2$ (i.e., $\delta l_\mathrm{I} = \delta l_\mathrm{II} = 0$, $\delta m_\mathrm{I} = -\delta m_\mathrm{II}$) that can be viewed as having opposite imaginary "*mass*" [65–68] (i.e., reversed *non-Hermitian order*), new interface modes emerge beyond the bulk bands in the absence of a band gap. In fact, they are generated via the EP and described by invariants called *vorticity* [69]. The corresponding waveguide schematics and interface mode distributions are shown in Fig. 2(d).

More discussions on the topological origins of the Weyl interface states are provided in Supplemental Material S2 [50].

Note that we have defined the two Weyl media with the same radii (δl_0, δm_0, and δn_0) in the parameter sphere, while only ϕ varies. However, the radii can also be tuned to be different. It has been theoretically proven that the WER shows completely distinct topological properties between inside and outside the ring [14,20], while the interface mode when interfacing a medium inside a WER with one outside a WER has not been observed by far. Inspired by it, two rotational loops are selected in the $\delta l - \delta m$ parameter space with different radii, e.g., $a_I \delta m_{0I} = 0.005$, $a_{II} \delta m_{0II} = 0.015$, so that Weyl medium-I rotating inside two EPs has gapped spectrum [Fig. 2(b)] corresponding to outside the WER, while Weyl medium-II rotating enclosing two EPs is ungapped and thus inside the WER [see Fig. 3(a)]. Figures 3(b) and 3(d) show the real and imaginary parts of eigenvalue spectra as a function of rotating angle ϕ_I ($\phi_I = \phi_{II}$), respectively. As expected, Weyl medium-I (outside the WER) has nontrivial gapped real spectrum (gray bands) and supports a localized Fermi arc like edge state (red curve) generated by the nontrivial Berry charge of the WER, while the real spectrum of the Weyl medium II (inside the WER) is gapless (brown bands). The edge mode reemerges as an interface state with the lowest loss in the vicinity of $\phi = \pi/2$ [see Fig. 3(d)], which cannot couple to both bulk bands due to the topological band gap of medium I and
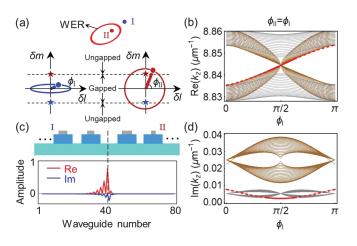

FIG. 3. (a) Two rotational loops of different sizes are introduced in $\delta l - \delta m$ spaces, where ϕ_I and ϕ_{II} are azimuthal angles that define the two synthetic Weyl media (I and II). Weyl medium I and II (blue and red dots) are outside and inside the WER (red circle). The real (b) and imaginary (d) part of the eigenvalue spectra for loops in (a) with $\phi_{II} = \phi_I$. The red curve represents the interface mode. (c) Schematics of the waveguide structure and field distributions of the interface states at $\phi_I = \pi/2$. Here, $a_I = 0.00576$ μm^{-1}, $a_{II} = 0.02247$ μm^{-1}, $\delta l_0 = 0.001$, and $\delta n_0 = -0.05$.

non-Hermiticity-induced decoupling with medium II (see Supplemental Material S2 [50]). In short, this interface mode is fundamentally generated by Berry flux emitting from the WER, and the non-Hermitian phase transitions crossing the WER guarantee the localized propagation of the interface modes, which can emerge even without mass transition ($\phi_I = \phi_{II}$). As a consequence, this interface state shows different features (asymmetric) compared to the interface modes with mass transition (symmetric) [see the mode distributions and corresponding waveguide schematics in Fig. 3(c)], which can be explained that these two Weyl media have different mass weights. These results give a new cognition to the origin of the non-Hermitian induced edge states [40,41,45–47].

In experiments, different Weyl media are constructed by controlling the silicon waveguide widths, Cr widths, and waveguide gaps. Specifically, three kinds of samples were fabricated corresponding to imaginary mass transition case, crossing WER case, and trivial Hermitian case (removing Cr) for comparison [see Figs. 4(a)–4(c)]. The imaginary mass transition corresponds to reverse the Cr width order at the interface, while the order remains the same but the two media have different Cr width contrast for the case crossing the WER. The experimental details including sample fabrication, measurement, and structure parameters are provided in Supplemental Material S3 [50]. We input the 1550 nm laser into the center of the three samples through a grating coupler and capture the output signals [see Figs. 4(e), 4(h), and 4(k)]. Numerical propagation simulations are also performed [see Figs. 4(d), 4(g), and 4(j)]. We extract the simulated output intensity (propagation length 200 μm) and display them in Figs. 4(f), 4(i), and 4(l) (green bar) along with experimentally measured intensity profiles (orange bars).

For the case with imaginary mass transition, we input the light from the central two waveguides according to the maximum-weighted field of the interface mode [see Fig. 2(d)]. Figure 4(d) shows the simulation result with a strong field confined around the interface, which is in good agreement with the experiments [see Figs. 4(e) and 4(f)]. For the case crossing WER, we choose the central waveguide as the input. The simulation in Fig. 4(g) indicates an overall interface mode, although some fields penetrate into the bulk. This small penetration should attribute to the discrepancy of the input field from the exact eigenmode profile [see Fig. 3(c)]. In Figs. 4(h) and 4(i), both the experiment and simulation exhibit a power maximum around the interface, which shows good coincidence with the theory prediction. For the trivial Hermitian case, the optical fields spread out into the bulk of the structure, showing no localized modes at the interface [Figs. 4(j)–4(l)]. More experimental data and further discussions about the robustness are provided in Supplemental Material S3 and S4 [50].
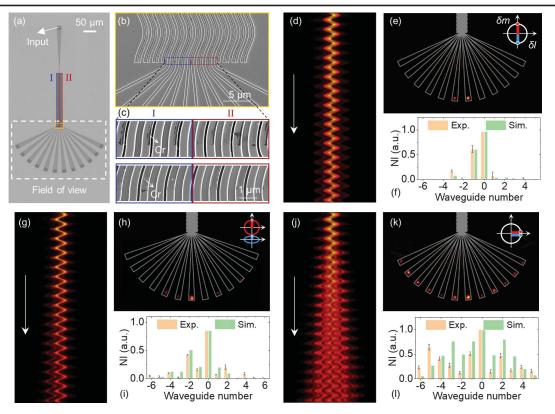
FIG. 4.   (a) SEM top view of a sample. (b) and (c) Enlarged regions. (d)–(f) Simulated light propagations (d), experimentally detected output intensities (e), and normalized intensity (NI) profiles (f) of simulation (green bars) and experimental results (orange bars) for the imaginary mass transition case. Corresponding results for crossing the WER case (g)–(i) and Hermitian trivial case (j)–(l).

In summary, we have explored the Weyl interface states in the Cr-deposited curved silicon waveguide array by imparting one non-Hermitian parameter space. Such a system can build high-dimensional Hamiltonians including non-Hermitian synthetic momenta with respect to the non-Hermitian order, and hence provides new possibilities to control the interface modes. New types of Weyl interface states are revealed, which are explained by sign-reversed imaginary mass (reversed *non-Hermitian order*) and phase transition crossing the WER with the same-sign mass. All of these results have been successfully observed in Si waveguide experiments, which show good agreement with the theory. The successful realization in the Si platform also indicates the possibility of non-Hermitian light manipulation for compact integrations. Moreover, our Letter extends the category of synthetic dimension with non-Hermiticity, which has demonstrated the powerful capability in tailoring the *non-Hermitian order* and promises further explorations in non-Hermitian and higher-dimensional physics.

[*]Corresponding author.
yuanluqi@sjtu.edu.cn
[†]Corresponding author.
taoli@nju.edu.cn

[1] T. Ozawa, H. M. Price, A. Amo, N. Goldman, M. Hafezi, L. Lu, M. C. Rechtsman, D. Schuster, J. Simon, O. Zilberberg, and I. Carusotto, Topological photonics, Rev. Mod. Phys. **91**, 015006 (2019).

[2] H. Price, Y. Chong, A. Khanikaev, H. Schomerus, L. J. Maczewsky, M. Kremer, M. Heinrich, A. Szameit, O. Zilberberg, and Y. Yang, Roadmap on topological photonics, J. Phys. Photonics **4**, 032501 (2022).

[3] L. Lu, Z. Wang, D. Ye, L. Ran, L. Fu, J. D. Joannopoulos, and M. Soljačić, Experimental observation of Weyl points, Science **349**, 622 (2015).

[4] L. Lu, L. Fu, J. D. Joannopoulos, and M. Soljačić, Weyl points and line nodes in gyroid photonic crystals, Nat. Photonics **7**, 294 (2013).

[5] W. Chen, M. Xiao, and C. T. Chan, Photonic crystals possessing multiple Weyl points and the experimental observation of robust surface states, Nat. Commun. **7**, 13038 (2016).

[6] B. Yang, Q. Guo, B. Tremain, R. Liu, L. E. Barr, Q. Yan, W. Gao, H. Liu, Y. Xiang, J. Chen, C. Fang, A. Hibbins, L. Lu, and S. Zhang, Ideal Weyl points and helicoid surface states in artificial photonic crystal structures, Science **359**, 1013 (2018).

[7] M. Xiao, Q. Lin, and S. Fan, Hyperbolic Weyl Point in Reciprocal Chiral Metamaterials, Phys. Rev. Lett. **117**, 057401 (2016).

[8] J. Noh, S. Huang, D. Leykam, Y. D. Chong, K. P. Chen, and M. C. Rechtsman, Experimental observation of optical Weyl points and Fermi arc-like surface states, Nat. Phys. 13, 611 (2017).

[9] X. Wan, A. M. Turner, A. Vishwanath, and S. Y. Savrasov, Topological semimetal and Fermi-arc surface states in the electronic structure of pyrochlore iridates, Phys. Rev. B 83, 205101 (2011).

[10] S.-Y. Xu et al., Discovery of a Weyl fermion semimetal and topological Fermi arcs, Science 349, 613 (2015).

[11] M. Xiao, W.-J. Chen, W.-Y. He, and C. T. Chan, Synthetic gauge flux and Weyl points in acoustic systems, Nat. Phys. 11, 920 (2015).

[12] H. He, C. Qiu, L. Ye, X. Cai, X. Fan, M. Ke, F. Zhang, and Z. Liu, Topological negative refraction of surface acoustic waves in a Weyl phononic crystal, Nature (London) 560, 61 (2018).

[13] F. Li, X. Huang, J. Lu, J. Ma, and Z. Liu, Weyl points and Fermi arcs in a chiral phononic crystal, Nat. Phys. 14, 30 (2018).

[14] Y. Xu, S. Wang, and L. Duan, Weyl Exceptional Rings in a Three-Dimensional Dissipative Cold Atomic Gas, Phys. Rev. Lett. 118, 045701 (2017).

[15] A. Cerjan, M. Xiao, L. Yuan, and S. Fan, Effects of non-Hermitian perturbations on Weyl Hamiltonians with arbitrary topological charges, Phys. Rev. B 97, 075128 (2018).

[16] Q. Yan, Q. Chen, L. Zhang, R. Xi, H. Chen, and Y. Yang, Unconventional Weyl exceptional contours in non-Hermitian photonic continua, Photonics Res. 9, 2435 (2021).

[17] Q. Wang, K. Ding, H. Liu, S. Zhu, and C. T. Chan, Exceptional cones in 4D parameter space, Opt. Express 28, 1758 (2020).

[18] W. Tang, X. Jiang, K. Ding, Y. Xiao, Z. Zhang, C. T. Chan, and G. Ma, Exceptional nexus with a hybrid topological invariant, Science 370, 1077 (2020).

[19] X. Zhang, K. Ding, X. Zhou, J. Xu, and D. Jin, Experimental Observation of an Exceptional Surface in Synthetic Dimensions with Magnon Polaritons, Phys. Rev. Lett. 123, 237202 (2019).

[20] A. Cerjan, S. Huang, M. Wang, K. P. Chen, Y. Chong, and M. C. Rechtsman, Experimental realization of a Weyl exceptional ring, Nat. Photonics 13, 623 (2019).

[21] A. B. Redondo, I. Andonegui, M. J. Collins, G. Harari, Y. Lumer, M. C. Rechtsman, B. J. Eggleton, and M. Segev, Topological Optical Waveguiding in Silicon and the Transition between Topological and Trivial Defect States, Phys. Rev. Lett. 116, 163901 (2016).

[22] J.-L. Tambasco, G. Corrielli, R. J. Chapman, A. Crespi, O. Zilberberg, R. Osellame, and A. Peruzzo, Quantum interference of topological states of light, Sci. Adv. 4, eaat3187 (2018).

[23] A. B. Redondo, B. Bell, D. Oren, B. J. Eggleton, and M. Segev, Topological protection of biphoton states, Science 362, 568 (2018).

[24] H. Zhao, P. Miao, M. H. Teimourpour, S. Malzard, R. ElGanainy, H. Schomerus, and L. Feng, Topological hybrid silicon microlasers, Nat. Commun. 9, 981 (2018).

[25] B. Bahari, A. Ndao, F. Vallini, A. El Amili, Y. Fainman, and B. Kanté, Nonreciprocal lasing in topological cavities of arbitrary geometries, Science 358, 636 (2017).

[26] O. Boada, A. Celi, J. I. Latorre, and M. Lewenstein, Quantum Simulation of an Extra Dimension, Phys. Rev. Lett. 108, 133001 (2012).

[27] T. Ozawa and H. M. Price, Topological quantum matter in synthetic dimensions, Nat. Rev. Phys. 1, 349 (2019).

[28] L. Yuan, Y. Shi, and S. Fan, Photonic gauge potential in a system with a synthetic frequency dimension, Opt. Lett. 41, 741 (2016).

[29] L. Yuan, Q. Lin, M. Xiao, and S. Fan, Synthetic dimension in photonics, Optica 5, 1396 (2018).

[30] A. Dutt, Q. Lin, L. Yuan, M. Minkov, M. Xiao, and S. Fan, A single photonic cavity with two independent physical synthetic dimensions, Science 367, 59 (2020).

[31] K. Wang, A. Dutt, K. Y. Yang, C. C. Wojcik, J. Yučković, and S. Fan, Generating arbitrary topological windings of a non-Hermitian band, Science 371, 1240 (2021).

[32] E. Lustig, S. Weimann, Y. Plotnik, Y. Lumer, M. A. Bandres, A. Szameit, and M. Segev, Photonic topological insulator in synthetic dimensions, Nature (London) 567, 356 (2019).

[33] M. Wimmer, H. M. Price, I. Carusotto, and U. Peschel, Experimental measurement of the Berry curvature from anomalous transport, Nat. Phys. 13, 545 (2017).

[34] X. Luo, X. Zhou, J. Xu, C. Li, G. Guo, C. Zhang, and Z. Zhou, Synthetic-lattice enabled all-optical devices based on orbital angular momentum of light, Nat. Commun. 8, 16097 (2017).

[35] Q. Lin, M. Xiao, L. Yuan, and S. Fan, Photonic Weyl point in a two-dimensional resonator lattice with a synthetic frequency dimension, Nat. Commun. 7, 13731 (2016).

[36] Q. Wang, M. Xiao, H. Liu, S. Zhu, and C. T. Chan, Optical Interface States Protected by Synthetic Weyl Points, Phys. Rev. X 7, 031032 (2017).

[37] Z. Yan, Q. Wang, M. Xiao, Y. Zhao, S. Zhu, and H. Liu, Probing Rotated Weyl Physics on Nonlinear Lithium Niobate-on-Insulator Chips, Phys. Rev. Lett. 127, 013901 (2021).

[38] X. Fan, C. Qiu, Y. Shen, H. He, M. Xiao, M. Ke, and Z. Liu, Probing Weyl Physics with One-Dimensional Sonic Crystals, Phys. Rev. Lett. 122, 136802 (2019).

[39] J. Liu, Z. Li, Z. Chen, W. Tang, A. Chen, B. Liang, G. Ma, and J. Cheng, Experimental Realization of Weyl Exceptional rings in a Synthetic Three-Dimensional Non-Hermitian Phononic Crystal, Phys. Rev. Lett. 129, 084301 (2022).

[40] Y. Li, C. Fan, X. Hu, Y. Ao, C. Lu, C. T. Chan, D. M. Kennes, and Q. Gong, Effective Hamiltonian for Photonic Topological Insulator with Non-Hermitian Domain Walls, Phys. Rev. Lett. 129, 053903 (2022).

[41] H. Zhao, X. Qiao, T. Wu, B. Midya, S. Longhi, and L. Feng, Non-Hermitian topological light steering, Science 365, 1163 (2019).

[42] H. Schomerus, Topologically protected midgap states in complex photonic lattices, Opt. Lett. 38, 1912 (2013).

[43] C. Poli, M. Bellec, U. Kuhl, F. Mortessagne, and H. Schomerus, Selective enhancement of topologically induced

interface states in a dielectric resonator chain, Nat. Commun. **6,** 6710 (2015).

[44] S. Weimann, M. Kremer, Y. Plotnik, Y. Lumer, S. Nolte, K. G. Makris, M. Segev, M. C. Rechtsman, and A. Szameit, Topologically protected bound states in photonic parity-time-symmetric crystals, Nat. Mater. **16,** 433 (2017).

[45] T. E. Lee, Anomalous Edge State in a Non-Hermitian Lattice, Phys. Rev. Lett. **116,** 133903 (2016).

[46] S. Malzard, C. Poli, and H. Schomerus, Topologically Protected Defect States in Open Photonic Systems with Non-Hermitian Charge-Conjugation and Parity-Time Symmetry, Phys. Rev. Lett. **115,** 200402 (2015).

[47] M. Pan, H. Zhao, P. Miao, S. Longhi, and L. Feng, Photonic zero mode in a non-Hermitian photonic lattice, Nat. Commun. **9,** 1308 (2018).

[48] S. Xia, D. Kaltsas, D. Song, I. Komis, J. Xu, A. Szameit, H. Buljan, K. G Makris, and Z. Chen, Nonlinear tuning of PT symmetry and non-Hermitian topological states, Science **372,** 72 (2021).

[49] Here the *non-Hermitian order* is defined to reflect the spatial arrangement of the non-Hermitian components.

[50] See Supplemental Material at http://link.aps.org/supplemental/10.1103/PhysRevLett.130.043803 for more details on the theory and experiment, which includes Refs. [51–53].

[51] A. D. Rakic, A. B. Djurisic, J. M. Elazar, and M. L. Majewski, Optical properties of metallic films for vertical-cavity optoelectronic devices, Appl. Opt. **37,** 5271 (1998).

[52] T. Fukui, Y. Hatsugai, and H. Suzuki, Chern numbers in discretized Brillouin zone: Efficient method of computing (spin) Hall conductances, J. Phys. Soc. Jpn. **74,** 1674 (2005).

[53] R. Zhao, G.-D. Xie, M. L. N. Chen, Z. Lan, Z. Huang, and W. E. I. Sha, First-principle calculation of Chern number in gyrotropic photonic crystals, Opt. Express **28,** 4638 (2020).

[54] A. Guo, G. J. Salamo, D. Duchesne, R. Morandotti, M. Volatier-Ravat, V. Aimez, G. A. Siviloglou, and D. N. Christodoulides, Observation of PT-Symmetry Breaking in Complex Optical Potentials, Phys. Rev. Lett. **103,** 093902 (2009).

[55] W. Song, W. Sun, C. Chen, Q. Song, S. Xiao, S. Zhu, and T. Li, Breakup and Recovery of Topological Zero Modes in Finite Non-Hermitian Optical Lattices, Phys. Rev. Lett. **123,** 165701 (2019).

[56] T. Pertsch, T. Zentgraf, U. Peschel, A. Brer, and F. Lederer, Anomalous Refraction and Diffraction in Discrete Optical Systems, Phys. Rev. Lett. **88,** 093901 (2002).

[57] N. K. Efremidis, P. Zhang, Z. Chen, D. N. Christodoulides, C. E. Rüter, and D. Kip, Wave propagation in waveguide arrays with alternating positive and negative couplings, Phys. Rev. A **81,** 053817 (2010).

[58] J. M. Zeuner, N. K. Efremidis, R. Keil, F. Dreisow, D. N. Christodoulides, A. Tünnermann, S. Nolte, and A. Szameit, Optical Analogues for Massless Dirac Particles and Conical Diffraction in One Dimension, Phys. Rev. Lett. **109,** 023602 (2012).

[59] Y. Lumer, M. A. Bandres, M. Heinrich, L. J. Maczewsky, H. Herzig-Sheinfux, A. Szameit, and M. Segev, Light guiding by artificial gauge fields, Nat. Photonics **13,** 339 (2019).

[60] W. Song, H. Li, S. Gao, S. Zhu, and T. Li, Subwavelength self-imaging in cascaded waveguide array, Adv. Photonics **2,** 034001 (2020).

[61] W. Song, T. Li, S. Wu, Z. Wang, C. Chen, Y. Chen, C. Huang, K. Qiu, S. Zhu, Y. Zou, and T. Li, Dispersionless Coupling Among Optical Waveguides by Artificial Gauge Field, Phys. Rev. Lett. **129,** 053901 (2022).

[62] D. Leykam, K. Y. Bliokh, C. Huang, Y. D. Chong, and F. Nori, Edge Modes, Degeneracies, and Topological Numbers in Non-Hermitian Systems, Phys. Rev. Lett. **118,** 040401 (2017).

[63] R. Jackiw and C. Rebbi, Solitons with fermion number 1/2, Phys. Rev. D **13,** 3398 (1976).

[64] K. Y. Bliokh, D. Leykam, M. Lein, and F. Nori, Topological non-Hermitian origin of surface Maxwell waves, Nat. Commun. **10,** 580 (2019).

[65] P.-S. Hsin, A. Kapustin, and R. Thorngren, Berry phase in quantum field theory: Diabolical points and boundary phenomena, Phys. Rev. B **102,** 245113 (2020).

[66] M. Ezawa, Electric circuit simulations of nth-Chern-number insulators in 2n-dimensional space and their non-Hermitian generalizations for arbitrary n, Phys. Rev. B **100,** 075423 (2019).

[67] G. Gonzalez, Dirac equation and optical wave propagation in one dimension, Phys. Status Solidi RRL **12,** 1700357 (2018).

[68] S. A. R. Horsley, Indifferent electromagnetic modes: Bound states and topology, Phys. Rev. A **100,** 053819 (2019).

[69] H. Shen, B. Zhen, and L. Fu, Topological Band Theory for Non-Hermitian Hamiltonians, Phys. Rev. Lett. **120,** 146402 (2018).